ACS Energy LETTERS

http://pubs.acs.org/journal/aelccp

Suppressing Auger Recombination of Perovskite Quantum Dots for Efficient Pure-Blue-Light-Emitting Diodes

Chenghao Bi, Zhiwei Yao, Jingcong Hu, Xingyu Wang, Mengqi Zhang, Shuyu Tian, Aqiang Liu, Yue Lu, Nora H. de Leeuw, Manling Sui, and Jianjun Tian*

Cite This: *ACS Energy Lett.* 2023, 8, 731−739

Read Online

ACCESS | Metrics & More | Article Recommendations | Supporting Information

ABSTRACT: **It is a big challenge to achieve pure-blue (≤470 nm) perovskite light-emitting diodes (PeLEDs) with high efficiency and stability. Here, we report pure-blue (electroluminescence at 469 nm) PeLEDs with a full width at half-maximum of 21 nm, high external quantum efficiency of 10.3%, luminance of 12 060 cd m^{-2}, and continuous operation half-life of 25 h, representing the state-of-the-art performance. This design is based on strongly quantum confined $CsPbBr_3$ quantum dots (QDs) with suppression of Auger recombination, which was enabled by inorganic ligands, replacing initial organic ligands on the QDs. The inorganic ligand acts as a "capacitor" to alleviate the charge accumulation and reduce the exciton binding energy of the QDs, which suppresses the Auger recombination, resulting in much lower efficiency roll-off of PeLEDs. Thus, the devices maintain high efficiency (>10%) at high luminance (>2000 cd m^{-2}), which is of considerable significance for the display application.**

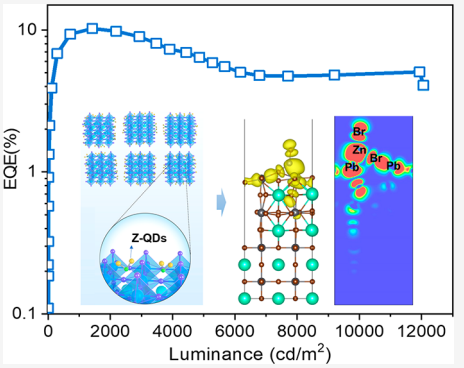

Metal halide perovskites have shown significant promise for application in light-emitting diodes (LEDs),[1−4] owing to their facile color tunability, narrow emission line widths, wide color range, as well as a cost-effective fabrication in solution.[5−10] In recent years, a tremendous increase in electroluminescence (EL) efficiency has been achieved for PeLEDs, with external quantum efficiencies (EQE) of more than 20% for red, green, and near-infrared emission wavelengths.[1−3,11,12] However, the performance of blue PeLEDs still lags far behind, although blue emission is a critical component in solid-state lighting and full-color displays.[13−20] As a result, much effort has been focused on constructing high-performance blue PeLEDs. Although state-of-art blue PeLEDs show EQEs of around 13%, their emission wavelengths within a range of 475−490 nm cannot meet the high blue purity emission (emitting wavelength below 470 nm with narrow emission band) requirements of solid-state lighting and displays.[5,7,21]

In principle, the blue emission of perovskites should be achieved easily through perovskite compositional engineering based on the Br/Cl mixed halides, but it suffers from halide segregation issues under an electric field, resulting in much poorer spectral and operational stabilities for the PeLEDs.[22−24] Recently, pure-blue PeLEDs based on small bromide-only perovskite QDs with diameters of ∼4 nm were obtained by utilizing the quantum confinement effect, which can avoid the mixed halides issue, thus achieving better operation stability and a continuous operational half-life (T_{50}) of several hours.[25−27] However, the soft and highly ionic lattice structures and low intrinsic formation energies of perovskites lead to ultrafast nucleation and growth rates of the QDs (they form via subsecond fast and hence hard-to-control ionic metathesis reactions). Therefore, it is challenging to obtain strongly confined pure-blue single-bromide perovskite QDs of uniform size and regular shape.[28,29] Furthermore, the pure-blue perovskite QDs are a strongly confined system comprising both quantum and dielectric confinement, which leads to the formation of strongly bound excitons and high exciton binding energies (E_b).[30,31] Rapid Auger recombination is proportional to E_b because of the enhanced Coulomb electron−hole interaction, which leads to carriers that are no longer uniformly distributed in space, thus raising the probability of finding two electrons and one hole at the same position to accelerate the Auger process, which results in the fast efficiency roll-off for

Received: November 17, 2022
Accepted: December 21, 2022
Published: December 28, 2022

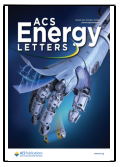

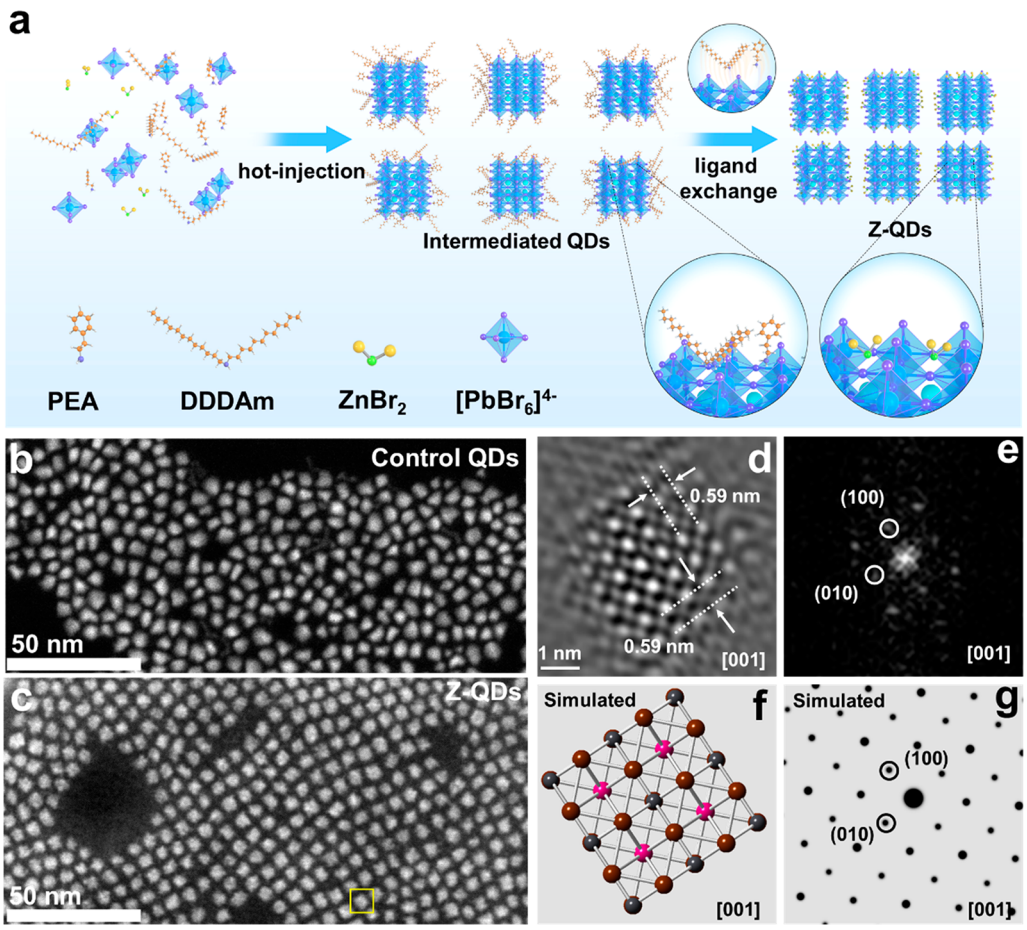

Figure 1. Morphology and structural characterization of QDs. (a) Schematic illustration of the Z-QD fabrication. Low-magnification HAADF-STEM images of the (b) control QDs and (c) Z-QDs. (d) Atomic-resolution HAADF-STEM images of the Z-QDs and (e) the corresponding FFT patterns, which arise from yellow box area in (c). Simulated (f) crystal structure and (g) FFT patterns of the Z-QDs based on data from (d).

the PeLEDs.[32−34] Thus, the EQE of the pure-blue PeLEDs based on QDs is much less than 10%.

Here, we report a route to synthesize strongly confined pure-blue $CsPbBr_3$ QDs in a rich Br^- ion environment by controlling the thermodynamic equilibrium (Figure 1a). The synthesized QDs are named as intermediate QDs in the following discussion. The introduction of $ZnBr_2$ could induce the strong binding of inorganic ligands to passivate uncoordinated sites and facilitate in situ partial exchange with the initial organic ligands of the intermediate QD surface, thus achieving $ZnBr_2$ inorganic ligands QD (Z-QD). The high intrinsic conductivity of the inorganic ligands will improve the charge mobility between adjacent Z-QDs. In addition, the larger dielectric constant of the inorganic ligands compared to the organic ligands can weaken the dielectric confinement and suppress Auger recombination. Thus, this strategy would effectively suppress nonradiative recombination of carriers in the QDs, including defect trapped recombination and Auger recombination.

In order to present the excellent performance of the Z-QDs, we have prepared pure-blue $CsPbBr_3$ QDs based on state-of-the-art pure-blue works, which are named as the control QDs in the following discussion. As shown in Figures 1b and S1, the scanning transmission electron microscopy (STEM) images of the control QDs exhibit irregular and inhomogeneous morphologies with a broad size distribution of 3.8 ± 0.8 nm (Figure S2). In contrast, the intermediate QDs and Z-QDs exhibit a more regular shape and uniform size distribution (3.7 ± 0.5 and 3.5 ± 0.3 nm, respectively), as shown in Figures S3 and 1c, which are attributed to the thermodynamic equilibrium of the excess Br^- between the crystal lattice and solution medium. Because Br^- is the most labile species in $CsPbBr_3$, thus diffusing with a low kinetic barrier within the lattice, the QD size would be most susceptible to the variation of Br^- ion equilibrium between the crystal and solution medium.[35−37] Excess Br^- ions could increase the kinetic barrier of Br^-, which induces homogeneous nucleation and growth. All the QDs show a much smaller size than the intrinsic exciton Bohr radius of $CsPbBr_3$ (~7 nm), further verifying the formation of strong quantum confinement, mentioned above.[36] As shown in Figures 1d and S1, the atomic-resolution high-angle annular dark field (HAADF) images of these QDs (yellow block area in Figure 1c) confirm that all have lattice spacings of 0.59 nm, corresponding to the (001) crystal plane of $CsPbBr_3$ and a cubic crystal structure (see fast Fourier transform (FFT) image and simulated results, inset to Figure 1e−g), which is consistent with the X-ray diffraction (XRD) results shown in Figure S4. The Z-QDs show nearly the same XRD patterns as the control QDs, without any noticeable peak shift. Energy dispersive X-ray spectroscopy (EDS) measurements show that the Cs:Pb:Br ratio also remains close to 1:1:3 for the intermediate QDs and Z-QDs (Tables S1 and S2), consistent

https://doi.org/10.1021/acsenergylett.2c02613
ACS Energy Lett. 2023, 8, 731−739

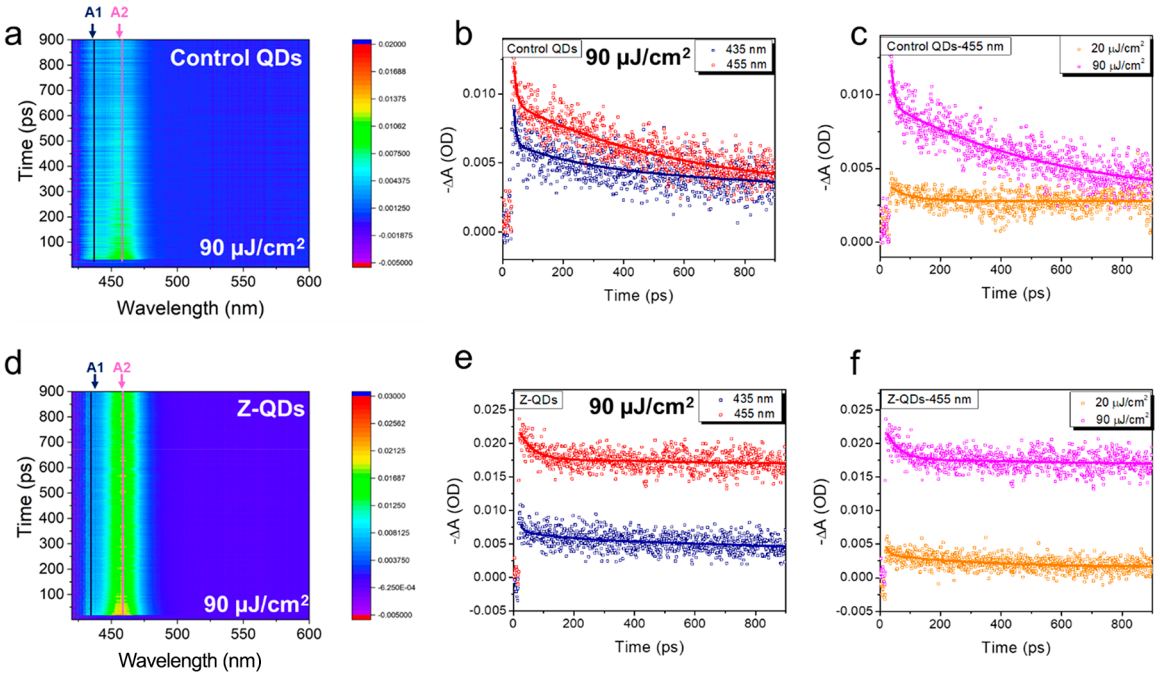

Figure 2. Photoexcited carrier dynamics analysis. Pseudocolor representation of transient absorption (TA) spectra of the (a) control QDs and (d) Z-QDs. Wavelength of pumping laser = 365 nm; pulse energy density ≈ 90 μJ/cm^2. Comparison of TA bleach recovery kinetics of the (b) QDs and (e) the Z-QDs monitored at 435 and 455 nm. Comparison of TA bleach recovery kinetics of the (c) control QDs and (f) Z-QDs under the monitored wavelength of 455 nm and pulse energy densities of 20 and 90 μJ/cm^2.

with the $CsPbBr_3$ composition being maintained rather than changing to some other stoichiometry. In addition, the adjacent Z-QDs exhibit a distance of ~1.2 nm (Figure S2d), which is shorter than that of the control QDs and intermediate QDs (2.2 nm, Figure S2b). The narrower interatomic distance indicates that the inorganic ligands successfully replace organic ligands on the surface, because the length of inorganic ligands is much shorter than that of organic ligands. EDS mapping further verifies the conclusion. As shown in Figures S5 and S6, Zn enrichment is observed between adjacent Z-QDs, but there is no Zn signal for the intermediate QDs, indicating that the Zn signal of the Z-QDs results from the inorganic ligands on the boundary of the Z-QDs, rather than from doping of $ZnBr_2$, thereby further demonstrating the successful ligand exchange between $ZnBr_2$ and organic ligands.

The UV−vis absorption and photoluminescence (PL) spectra results (Figures S7a−c and S8) demonstrate that all the QDs exhibit the similar band-edge excitonic absorption and PL peaks, located at 455 and 460 nm wavelengths, respectively. The intermediated QDs and Z-QDs show a narrower full width at half-maximum (fwhm) of the PL (19 nm) than the control QDs (28 nm), which is consistent with the more uniform size distribution, owing to the metal-halide-controlled thermodynamic equilibrium. The PL quantum yield (PLQY) of the Z-QDs is near unity (99%), which is slightly higher than that of the control QDs, demonstrating the lower trap density for the Z-QDs. As shown in Figure S7e, the Urbach energy of the Z-QDs (27 meV) is slightly smaller than that of the control QDs (30 meV), further demonstrating the much lower trap density for the Z-QDs. The time-resolved PL (TRPL) decay was carried out to further study the trap density of the QDs (Figure S7d and Table S3). The control and Z-QDs exhibit similar near single-exponential carrier decay dynamics, while the average PL lifetime of the Z-QDs is 12.2 ns, i.e., longer than that of the control QDs (10.7 ns). The Z-QDs also exhibit a slower apparent nonradiative rate (8.0×10^{-4} ns^{-1}) compared to the control QDs (8.0×10^{-3} ns^{-1}). These results indicate that the inorganic ligands could passivate surface defects more effectively, suppressing defect trapped nonradiative recombination.

Femtosecond transient absorption (fs-TA) measurements were performed to elucidate the mechanism underlying the superb photophysical properties of the Z-QDs. Both the control QDs and Z-QDs present two noticeable negative probe bleaching (PB) peaks at 435 and 455 nm (A1 and A2) (Figure 2a,d). The A2 peak is consistent with the steady absorption, which is attributed to the ground state bleaching (GSB) of the band-edge excitonic state, and the mechanism by which it bleaches is typically attributed to state-filling.[29,38] The A1 peak is ascribed to the high-energy exciton transition.[37] Next, we adjusted the pump intensity to study a different dynamic process in the QDs, and Figures 2a−f and S9 clearly show the distinguishing decay process of the control QD and Z-QD films at different pump intensities of up to 90 μJ/cm^2. It is clearly seen that the decay process becomes fast when the pump intensity is larger than 30 μJ/cm^2. This observation indicates the presence of a serious Auger recombination process in control QDs. The control QDs were characterized by biexponential bleach recovery dynamics when the pump intensity increases to 90 μJ/cm^2, exhibiting a fast component of 12.6 ps (τ_1, 63.3%) and a long component of 561.7 ps (τ_2, 36.7%), in which τ_1 can be attributed to the Auger process occurring on the same dot (intradot Auger recombination) or trap-assisted Auger recombination. For τ_2, the longer hundreds of picoseconds component arises from diffusion-assisted Auger processes in a thin film.[39] However, the exciton recovery dynamics of the Z-QDs is almost independent from the pump intensity (Figures 2d−f and S9b). The decay reaction of the Z-QDs exhibits near single-exponential decay dynamics (Figure S10 and Table S5), with two time constants of 46.9 ps (τ_1,

https://doi.org/10.1021/acsenergylett.2c02613
ACS Energy Lett. 2023, 8, 731−739

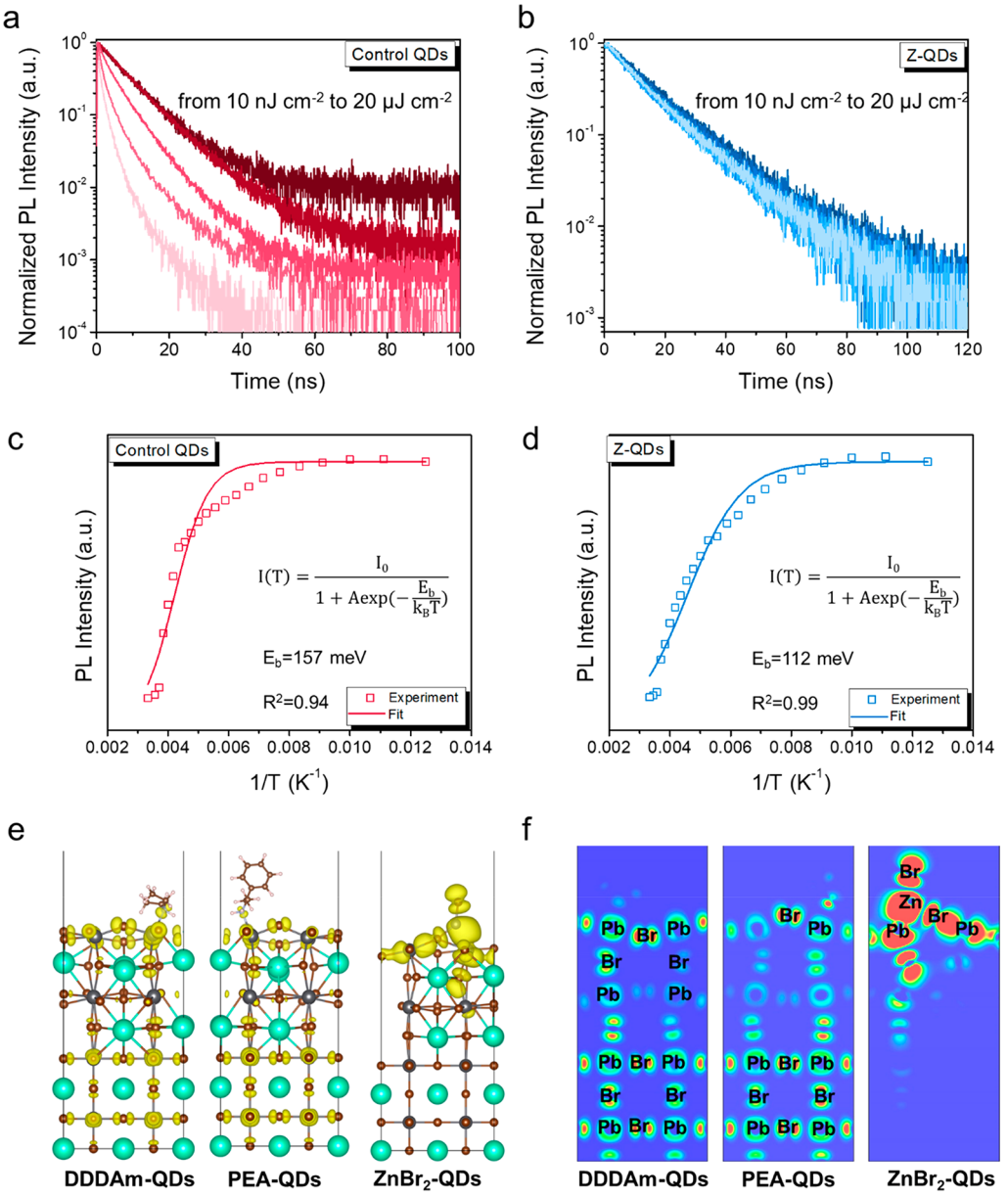

Figure 3. Auger recombination for Z-QDs. Time-resolved PL decay spectra of (a) QDs and (b) Z-QDs with different excitation. Integrated PL intensity of the (c) control QDs and (d) Z-QDs as a function of reciprocal temperature. (e,f) DFT calculation of electronic charge density with an additional two electrons under an external electronic field near the valence band (yellow) for DDDAm-QDs, PEA-QDs, and $ZnBr_2$-QDs.

7.4%) and 5626 ps (τ_2, 92.6%), which suggest that the Auger recombination is suppressed in the Z-QDs. To exempt traps as the reason for the different TA kinetics based on the pump-intensity-dependence TA spectra, the TA response with low pump intensity (20 μJ/cm^2) was also carried out, as shown in Figure S11, because the Auger recombination in the QD can be negligible under low-power intensity.[40] However, the decay reaction of the two QDs exhibits almost the same approximately single-exponential decay dynamics with the time constants used (Table S4), suggesting negligible electron or hole trapping pathways in the two QDs, and the trap state density is therefore not the key factor determining the excellent properties of the Z-QDs. Thus, the above results indicate the presence of a strong intradot or diffusion-assisted Auger recombination process in the control QDs under the high-pump-intensity excitation, while the Auger recombination may be effectively suppressed in the Z-QDs.

Global fitting was carried out to simultaneously simulate all the kinetics for the QDs (Figure S12). The fitted kinetics indicate that the GSB mainly consists of three photophysical processes,[41,42] in which the hot electrons relax from the excited states to the bottom of the conduction band on the femtosecond time scale.[43] The slightly longer component is attributed to the Auger recombination (hundreds of picoseconds stemming from diffusion-assisted Auger recombination, whereas intradot Auger may still exist) and the trap-assisted nonradiative recombination occurs on the picosecond time scale.[44] The nanosecond components are obviously derived from the intrinsic edge exciton radiative recombination and are consistent with the steady-state PL lifetime.[45] Weaker bleaching intensity and longer kinetic times of the Z-QDs

https://doi.org/10.1021/acsenergylett.2c02613
ACS Energy Lett. 2023, 8, 731−739

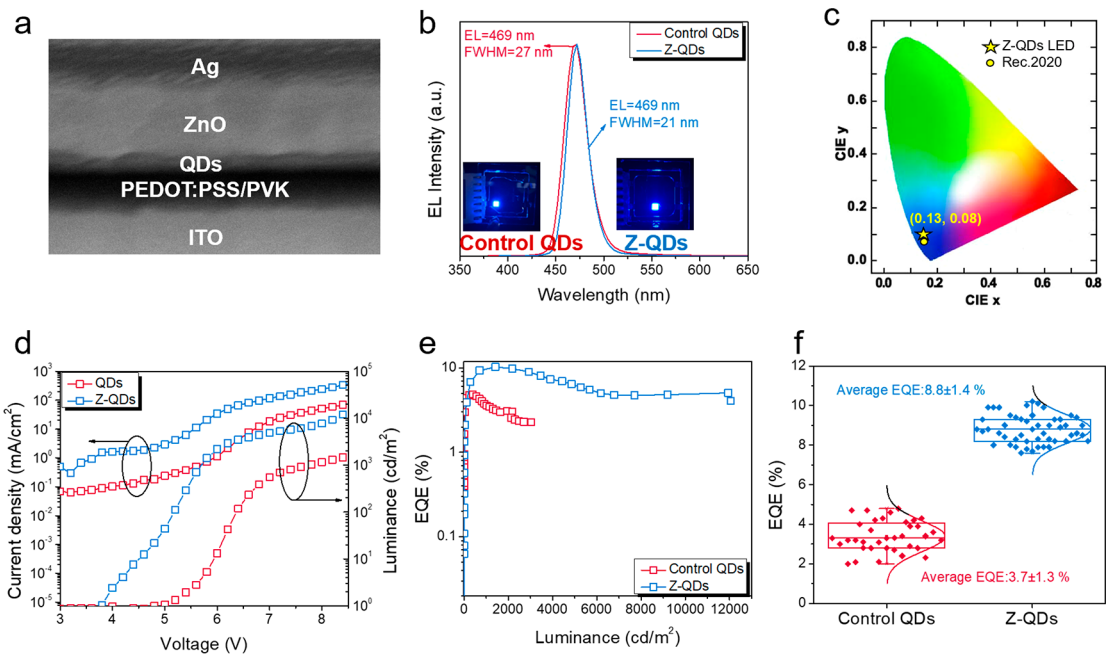

Figure 4. Performance of PeLEDs based on Z-QDs. (a) STEM cross-section view image of device. (b) EL of the PeLEDs and (c) the CIE coordinates of the PeLEDs. Inset in (b) shows the digital photo of the PeLEDs operated under a current density of 4 V. (d) Current density and luminance of the PeLEDs versus bias. (e) EQE of the PeLEDs versus luminance. (f) Box plot of the maximum EQE of PeLEDs based on control QDs and Z-QDs.

indicate that the Auger recombination has been effectively inhibited. In addition, the relative intensity ratio of A1/A2 of the Z-QDs is smaller than that of the control QDs, indicating that the high-energy excitons in the Z-QDs could are relaxed easily to the band edge, which is of benefit to alleviate the accumulation of high-energy excitons inside the QDs, thus suppressing the Auger recombination process.

To further verify the suppressed Auger recombination in the Z-QDs, excitation-intensity-dependent TRPL spectra were obtained. As can be clearly seen from Figure 3a, the decay process rate increases with the increase of excitation intensity, and the carrier dynamics also changes from single-exponential decay to triexponential decay, due to the significant Auger recombination process in the control QDs under high excitation intensity.[34] In contrast, there is no change for the TRPL spectra of the Z-QDs (Figure 3b), even if the intensity is increased to 20 μJ/cm^2, indicating the absence of Auger recombination in the Z-QDs under high carrier density. The trimolecular Auger recombination constant is an order of magnitude lower for the Z-QDs compared to the control QDs. To understand fully the exciton dynamics of two samples, we first carried out the temperature dependence of PL measurements, shown in Figures 3c,d and S13. The extracted E_b is estimated to be 157 and 112 meV for the control and Z-QDs, respectively, which suggests that the suppressed Auger recombination might result from the decreased E_b, because the dielectric constant of the inorganic ligand is close to $CsPbBr_3$, which reduces the dielectric confinement. Moreover, the temperature-dependent PL FHWM has an important influence on the excitonic PL emissions and can provide information about the interaction of excitons with optical or acoustic phonons.[46] As presented in the Figure S13, the optical phonon energy (γ_{LO}) of the Z-QDs (317.7 meV) is much lower than that of the control QDs (374.4 meV), verifying the effectively suppressed exciton−phonon interaction in the Z-QDs, thereby enabling the radiative recombination with considerable PL efficiency.

To further clarify the mechanism of the suppressed Auger recombination, we have carried out first-principle calculations based on the density functional theory (DFT). First, we simulated the QD surfaces with different adsorbates and without any external field (EF). It is observed that the inorganic ligand exhibits a stronger coordination interaction with the QDs than that of the initial organic ligands (Figure S14). Furthermore, no obvious differences in the partial charge density, as shown in Figure S15, demonstrate their similar PL behaviors, which is consistent with the experimental results. To research the EL properties of the surfaces with different adsorbates, the plot of the partial charge density of the QDs with EF and additional electrons has been depicted in Figures 3e,f and S15−17. For the surfaces with the initial organic adsorbates (PEA and DDDAm), the charge density near the valence band maximum (VBM) and conduction band minimum (CBM) is distributed over all the layers from the bottom to the top, including the adsorbates, while in the surface with inorganic ligands, the charge density near the VBM in the subtop and bottom layers has decreased (Figure 3f), and instead, a remarkable concentration of the charge in the top layer adjacent to the inorganic ligand is observed near its Fermi level, illustrating that the inorganic adsorbate could act as a "capacitor" and attract the charge in the subtop layers and concentrate it in the surrounding area, which would reduce the accumulation of carriers inside QDs and suppress the possibility of Auger recombination. By combining the above DFT calculations with the temperature-dependent PL spectra, we conclude that the capacitive action of the inorganic ligand effectively decreases E_b and inhibits Auger recombination. This behavior can reversibly store and release electrons driven by the partial electronic density of states redistribution,

https://doi.org/10.1021/acsenergylett.2c02613
ACS Energy Lett. 2023, 8, 731−739

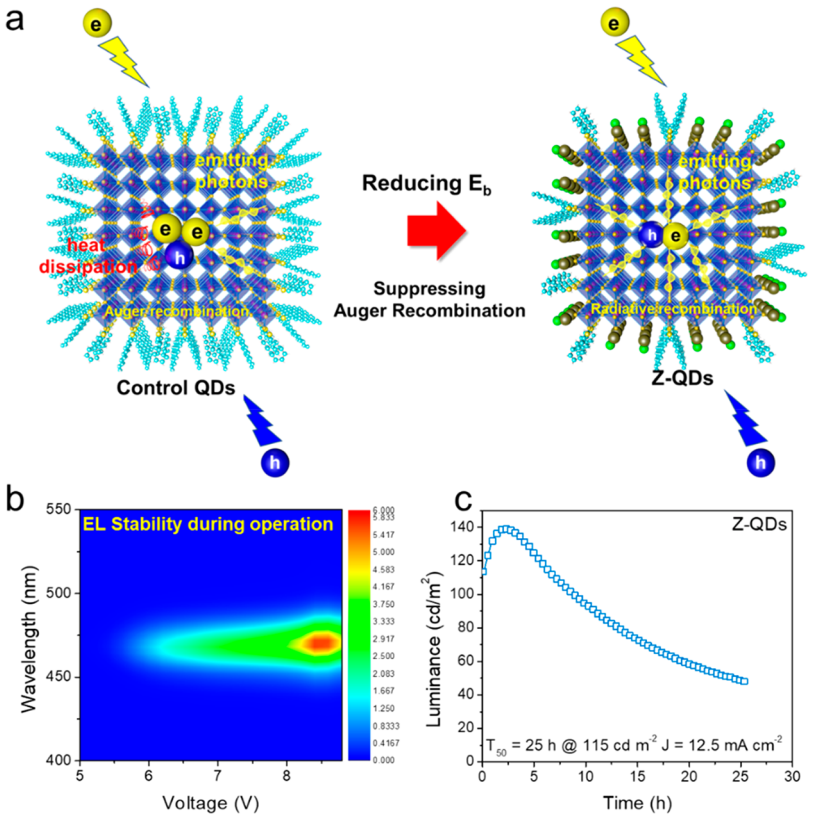

Figure 5. Depression mechanism of Auger recombination and stability of PeLEDs. (a) Schematic illustration of suppressed Auger recombination in the QDs. (b) EL spectra of the PeLEDs at different operating voltages. (c) The operational half-lifetime T_{50} of the PeLEDs at an initial luminance of 115 cd m^{-2}.

which enhances the delocalization of electrons in QDs and thus suppresses QD charging at high carrier concentrations.[47]

The all solution-processed LEDs show potential low-cost manufacture in comparison with conventional LEDs prepared by metal organic chemical vapor deposition, but the perovskite layer is easily destroyed by the solution process, resulting in much poorer performance. Our Z-QDs exhibit remarkable high stability (Figure S18), which can resist the destruction of the subsequent polar solvent deposition, which is attributed to the strong binding between inorganic ligands and QDs. We have prepared the PeLEDs in a configuration of indium tin oxide (ITO)-coated glass, poly(3,4-ethylenedioxythiophene) polystyrenesulfonate (PEDOT:PSS), polyvinylcarbazole (PVK), perovskite QDs, ZnO nanoparticles, and silver (Ag). Note that, except for the thermal-evaporated top Ag electrode, all other layers were spin-coated from solutions. Figure 4a shows a STEM image of a cross-section of a device, which reveals a well-defined multilayer structure. The device based on Z-QDs shows a symmetric pure-blue EL peak at 469 nm with an fwhm of 21 nm (Figure 4b), corresponding to CIE (Commission Internationale de l'Eclairage) color coordinates of (0.13, 0.08), which meets the standards of the National Television System Committee (NTSC) and approaches the new Rec. 2020 standards (Figure 4c), thus representing an ideal blue emission for display applications. The narrow EL is attributed to the uniform size distribution of the Z-QDs, resulting in high-purity blue emission. The current density–voltage-luminance (J–V–L) curves of the devices are shown in Figure 4d, and the corresponding EQE results are shown in Figure 4e. The turn-on voltage (V_{TO}) (V_{TO} is generally defined as the applied voltage necessary to detect the luminance of 1 cd m^{-2}) of the PeLED based on Z-QDs is 3.7 V, which is lower than that of the control device (4.3 V). The PeLEDs based on the Z-QDs film show a higher current density at the same voltage and a faster rising trend in luminance with operating voltage than those of the control PeLEDs, which is attributed to the higher intrinsic conductivity of the inorganic ligands.[48] The maximum luminance of the PeLED based on the Z-QDs is 12 060 cd m^{-2}, which is a record value compared to the state-of-art pure-blue PeLEDs. We calculated a maximum EQE of 10.3% at the current density of 20.9 mA/cm^2 for the PeLEDs with QDs, while the control PeLEDs show a peak EQE of 4.8% (Figure 4e).

The EQE and luminance of the Z-QD PeLEDs represent new records for pure-blue PeLEDs with emission below 470 nm (Table S6). Importantly, the PeLEDs based on the Z-QDs show much lower efficiency roll-off than that of the control QDs at high current density and luminance and maintain an EQE over 10% even at 2000, thus achieving high efficiency at high luminance, which is of major significance for display applications, demonstrating the lesser Auger recombination of the Z-QD PeLED. Statistical results from 30 devices (Figure 4f) confirm that the average maximum luminance and peak EQE of the PeLEDs with Z-QDs (8.8%) are better than those of the control devices (3.7%). The average maximum luminance of the PeLEDs with Z-QDs (9590 cd m^{-2}) is also much higher than that of the control devices (2630 cd m^{-2}) (Figure S19). It suggests that the vast improvement in the performance of the PeLED is due to the inorganic ligand, which not only inhibits Auger recombination but also improves carrier mobility (small dot distance).[32] The carrier mobility and energy level alignment of the QD film are related to the

https://doi.org/10.1021/acsenergylett.2c02613
ACS Energy Lett. 2023, 8, 731−739

charge injection balance of the PeLEDs. The Z-QD films exhibit a better energy level alignment, with elimination of the hole injection barrier in LEDs (Figure S20). Z-QD films exhibit the low trap density as the calculated results shown in Figure S21, indicating the great quality of Z-QD films. Z-QD films also exhibit smaller differences between the electron and hole mobilities, indicating better charge injection balance within the Z-QD film than in the control QD film (Figures S21 and 22).

As shown in Figure 5a, the control QDs shows the strong quantum confinement and the dielectric constant mismatch between inorganic QDs and surrounding organic ligands. Basically, the much lower polarity organic ligands with small dielectric constants could decrease the dielectric screening of the electron−hole Coulomb interaction, which induces the dielectric confinement. This leads to the formation of strongly bound excitons and high E_b. Rapid Auger recombination is proportional to the intensity of E_b because of the enhanced Coulomb electron−hole interaction, which leads to carriers' accumulation, thus enlarging the probability of finding two electrons and one hole at the same position to accelerate the Auger process. There is serious heat dissipation inside the control QDs because of the Auger process, which is harmful for the performance and operational stability of PeLEDs. After ligand exchange by inorganic ligands, the larger dielectric constant of inorganic ligands than that of organic ligands weakens the dielectric confinement. The E_b of the Z-QDs is obviously decreased. In addition, the inorganic ligand could effectively attract electrons and alleviate the charge accumulation in the Z-QDs. Lastly, both the intrinsic high conductivity of the inorganic ligands and reduced interatomic distance between the adjacent Z-QDs will improve the charge mobility of the Z-QD film, which further alleviates the charge accumulation in the device. Hence, Auger recombination in the Z-QDs was effectively suppressed.

Stability and operation lifetime are key factors for the application of PeLEDs. Notably, the EL of these PeLEDs exhibits excellent spectral stability during device operation, with negligible change in the emission peak and shape of the EL spectra even at a high voltage of 9 V (Figure 5b). We only detected a slight red-shift in the EL spectra when the luminance is increased to over 10 000 cd m^{-2}, which is caused by current-induced Joule heating and the quantum confined Stark effect, as revealed in previous work on cadmium chalcogenide QD LEDs.[49] We also performed an operational stability test under a constant driving current density of 12.5 mA cm^{-2}, which generates an initial luminance of 115 cd m^{-2}. Significantly, we measured an operational half-life T_{50} of 25 h (Figure 5c), with negligible change in the emission wavelength and shape of the EL spectra (Figure S23), which represents a remarkable improvement in comparison with the state-of-the-art stability performance of the blue PeLEDs (Table S6). The excellent operational stability of PeLEDs is assigned to the stable inorganic ETL, which could protect the perovskite emitters from the attack of H_2O and O_2.

In summary, we have reported a novel strategy to achieve strongly confined pure-blue-emitting perovskite $CsPbBr_3$ QDs with suppressed Auger recombination. A ligand exchange process between the inorganic ligand and organic ligands was performed to enable near-unity PLQY (99%). DFT calculations verified that the inorganic ligand could act as a "capacitor", which effectively attracts electrons and alleviates the charge accumulation in QDs. In addition, the close dielectric constant between the inorganic ligands and $CsPbBr_3$ decreased E_b, and thus, the Auger recombination process in the Z-QDs was significantly suppressed. With this strategy, the PeLEDs based on Z-QDs presented a pure-blue emission at 469 nm wavelength with a narrow fwhm (21 nm), low roll-off EQE, remarkably high luminance of 12 060 cd m^{-2}, and an EQE of 10.3%, representing the best performance so far for reported pure-blue PeLEDs with emission below 470 nm wavelength. The operating half-lifetime at 115 cd/m^2 is up to 25 h. In addition, the devices could maintain >10% EQE even at high luminance (2000 cd m^{-2}), which is of great significance for display applications.

■ ASSOCIATED CONTENT

Supporting Information

The Supporting Information is available free of charge at https://pubs.acs.org/doi/10.1021/acsenergylett.2c02613.

Materials and experimental methods of QD synthesis, PeLED fabrication, computational DFT calculations, QD and device characterization, SCLC characterization, calculation of exciton binding energy, fitting model of exciton−phonon coupling constant and EQE calculations, HAADF-STEM images, size distribution, XRD patterns, EDS mapping, absorption, PL, PL decay, Urbach energy diagram, TA spectra, temperature-dependent PL spectra, DFT simulated results, PLQY stability, UPS spectra, SCLC patterns, EL spectral stability, and device performance curves, including Figures S1−S23, Table S1−S6, and references (PDF)

■ AUTHOR INFORMATION

Corresponding Author

Jianjun Tian − *Institute for Advanced Materials and Technology and Shunde Innovation School, University of Science and Technology Beijing, Beijing 100083, China;* orcid.org/0000-0002-4008-0469; Email: tianjianjun@mater.ustb.edu.cn

Authors

Chenghao Bi − *Institute for Advanced Materials and Technology, University of Science and Technology Beijing, Beijing 100083, China*

Zhiwei Yao − *Institute for Advanced Materials and Technology, University of Science and Technology Beijing, Beijing 100083, China*

Jingcong Hu − *Beijing Key Laboratory of Microstructure and Properties of Solids, Institute of Microstructure and Properties of Advanced Materials, Beijing University of Technology, Beijing 100124, China*

Xingyu Wang − *School of Chemistry, University of Leeds, Leeds LS2 9JT, U.K.*

Mengqi Zhang − *Institute for Advanced Materials and Technology, University of Science and Technology Beijing, Beijing 100083, China*

Shuyu Tian − *Institute for Advanced Materials and Technology, University of Science and Technology Beijing, Beijing 100083, China*

Aqiang Liu − *Institute for Advanced Materials and Technology, University of Science and Technology Beijing, Beijing 100083, China*

Yue Lu − *Beijing Key Laboratory of Microstructure and Properties of Solids, Institute of Microstructure and Properties*

https://doi.org/10.1021/acsenergylett.2c02613
ACS Energy Lett. 2023, 8, 731−739

of Advanced Materials, Beijing University of Technology, Beijing 100124, China; orcid.org/0000-0001-9800-3792

Nora H. de Leeuw − *School of Chemistry, University of Leeds, Leeds LS2 9JT, U.K.; Department of Earth Sciences, Utrecht University, 3584 CB Utrecht, The Netherlands;* orcid.org/0000-0002-8271-0545

Manling Sui − *Beijing Key Laboratory of Microstructure and Properties of Solids, Institute of Microstructure and Properties of Advanced Materials, Beijing University of Technology, Beijing 100124, China;* orcid.org/0000-0002-0415-5881

Complete contact information is available at: https://pubs.acs.org/10.1021/acsenergylett.2c02613

Author Contributions

C.B., Z.Y., and J.H. contributed equally to this work.

Notes

The authors declare no competing financial interest.

■ ACKNOWLEDGMENTS

This work was supported by the Beijing Municipal Natural Science Foundation (2222061), Guangdong Basic and Applied Basic Research Foundation (2022A1515140007), National Natural Science Foundation of China (51961135107, 51774034, 51772026, 11704015, 51621003, 12074016), National Key Research and Development Program of China (2017YFE0119700), Beijing Innovation Team Building Program, China (IDHT20190503), Scientific Research Key Program of Beijing Municipal Commission of Education, China (KZ201310005002).

■ REFERENCES

(1) Cao, Y.; Wang, N.; Tian, H.; Guo, J.; Wei, Y.; Chen, H.; Miao, Y.; Zou, W.; Pan, K.; He, Y.; Cao, H.; Ke, Y.; Xu, M.; Wang, Y.; Yang, M.; Du, K.; Fu, Z.; Kong, D.; Dai, D.; Jin, Y.; Li, G.; Li, H.; Peng, Q.; Wang, J.; Huang, W. Perovskite light-emitting diodes based on spontaneously formed submicrometre-scale structures. *Nature* **2018**, *562* (7726), 249−253.

(2) Lin, K.; Xing, J.; Quan, L. N.; de Arquer, F. P. G.; Gong, X.; Lu, J.; Xie, L.; Zhao, W.; Zhang, D.; Yan, C.; Li, W.; Liu, X.; Lu, Y.; Kirman, J.; Sargent, E. H.; Xiong, Q.; Wei, Z. Perovskite light-emitting diodes with external quantum efficiency exceeding 20%. *Nature* **2018**, *562* (7726), 245−248.

(3) Ma, D.; Lin, K.; Dong, Y.; Choubisa, H.; Proppe, A. H.; Wu, D.; Wang, Y. K.; Chen, B.; Li, P.; Fan, J. Z.; Yuan, F.; Johnston, A.; Liu, Y.; Kang, Y.; Lu, Z. H.; Wei, Z.; Sargent, E. H. Distribution control enables efficient reduced-dimensional perovskite LEDs. *Nature* **2021**, *599* (7886), 594−598.

(4) Kovalenko, M. V.; Protesescu, L.; Bodnarchuk, M. I. Properties and potential optoelectronic applications of lead halide perovskite nanocrystals. *Science* **2017**, *358* (6364), 745−750.

(5) Karlsson, M.; Yi, Z.; Reichert, S.; Luo, X.; Lin, W.; Zhang, Z.; Bao, C.; Zhang, R.; Bai, S.; Zheng, G.; Teng, P.; Duan, L.; Lu, Y.; Zheng, K.; Pullerits, T.; Deibel, C.; Xu, W.; Friend, R.; Gao, F. Mixed halide perovskites for spectrally stable and high-efficiency blue light-emitting diodes. *Nat. Commun.* **2021**, *12* (1), 361.

(6) Sun, C.; Jiang, Y.; Cui, M.; Qiao, L.; Wei, J.; Huang, Y.; Zhang, L.; He, T.; Li, S.; Hsu, H. Y.; Qin, C.; Long, R.; Yuan, M. High-performance large-area quasi-2D perovskite light-emitting diodes. *Nat. Commun.* **2021**, *12* (1), 2207.

(7) Dong, Y.; Wang, Y. K.; Yuan, F.; Johnston, A.; Liu, Y.; Ma, D.; Choi, M. J.; Chen, B.; Chekini, M.; Baek, S. W.; Sagar, L. K.; Fan, J.; Hou, Y.; Wu, M.; Lee, S.; Sun, B.; Hoogland, S.; Quintero-Bermudez, R.; Ebe, H.; Todorovic, P.; Dinic, F.; Li, P.; Kung, H. T.; Saidaminov, M. I.; Kumacheva, E.; Spiecker, E.; Liao, L. S.; Voznyy, O.; Lu, Z. H.; Sargent, E. H. Bipolar-shell resurfacing for blue LEDs based on strongly confined perovskite quantum dots. *Nat. Nanotechnol.* **2020**, *15* (8), 668−674.

(8) Liu, M.; Wan, Q.; Wang, H.; Carulli, F.; Sun, X.; Zheng, W.; Kong, L.; Zhang, Q.; Zhang, C.; Zhang, Q.; Brovelli, S.; Li, L. Suppression of temperature quenching in perovskite nanocrystals for efficient and thermally stable light-emitting diodes. *Nat. Photonics* **2021**, *15* (5), 379−385.

(9) Wang, N.; Cheng, L.; Ge, R.; Zhang, S.; Miao, Y.; Zou, W.; Yi, C.; Sun, Y.; Cao, Y.; Yang, R.; Wei, Y.; Guo, Q.; Ke, Y.; Yu, M.; Jin, Y.; Liu, Y.; Ding, Q.; Di, D.; Yang, L.; Xing, G.; Tian, H.; Jin, C.; Gao, F.; Friend, R. H.; Wang, J.; Huang, W. Perovskite light-emitting diodes based on solution-processed self-organized multiple quantum wells. *Nat. Photonics* **2016**, *10* (11), 699−704.

(10) Xu, W.; Hu, Q.; Bai, S.; Bao, C.; Miao, Y.; Yuan, Z.; Borzda, T.; Barker, A. J.; Tyukalova, E.; Hu, Z.; Kawecki, M.; Wang, H.; Yan, Z.; Liu, X.; Shi, X.; Uvdal, K.; Fahlman, M.; Zhang, W.; Duchamp, M.; Liu, J.-M.; Petrozza, A.; Wang, J.; Liu, L.-M.; Huang, W.; Gao, F. Rational molecular passivation for high-performance perovskite light-emitting diodes. *Nat. Photonics* **2019**, *13* (6), 418−424.

(11) Hassan, Y.; Park, J. H.; Crawford, M. L.; Sadhanala, A.; Lee, J.; Sadighian, J. C.; Mosconi, E.; Shivanna, R.; Radicchi, E.; Jeong, M.; Yang, C.; Choi, H.; Park, S. H.; Song, M. H.; De Angelis, F.; Wong, C. Y.; Friend, R. H.; Lee, B. R.; Snaith, H. J. Ligand-engineered bandgap stability in mixed-halide perovskite LEDs. *Nature* **2021**, *591* (7848), 72−77.

(12) Chiba, T.; Hayashi, Y.; Ebe, H.; Hoshi, K.; Sato, J.; Sato, S.; Pu, Y.-J.; Ohisa, S.; Kido, J. Anion-exchange red perovskite quantum dots with ammonium iodine salts for highly efficient light-emitting devices. *Nat. Photonics* **2018**, *12* (11), 681−687.

(13) Liu, X. K.; Xu, W.; Bai, S.; Jin, Y.; Wang, J.; Friend, R. H.; Gao, F. Metal halide perovskites for light-emitting diodes. *Nat. Mater.* **2021**, *20* (1), 10−21.

(14) Liu, A.; Bi, C.; Guo, R.; Zhang, M.; Qu, X.; Tian, J. Electroluminescence Principle and Performance Improvement of Metal Halide Perovskite Light-Emitting Diodes. *Advanced Optical Materials* **2021**, *9* (18), 2002167.

(15) Lu, M.; Zhang, Y.; Wang, S.; Guo, J.; Yu, W. W.; Rogach, A. L. Metal Halide Perovskite Light-Emitting Devices: Promising Technology for Next-Generation Displays. *Adv. Funct. Mater.* **2019**, *29* (30), 1902008.

(16) Gangishetty, M. K.; Hou, S.; Quan, Q.; Congreve, D. N. Reducing Architecture Limitations for Efficient Blue Perovskite Light-Emitting Diodes. *Adv. Mater.* **2018**, *30* (20), 1706226.

(17) Zhang, X.; Wang, H.; Hu, Y.; Pei, Y.; Wang, S.; Shi, Z.; Colvin, V. L.; Wang, S.; Zhang, Y.; Yu, W. W. Strong Blue Emission from $Sb^{(3+)}$-Doped Super Small $CsPbBr_3$ Nanocrystals. *journal of physical chemistry letters* **2019**, *10* (8), 1750−1756.

(18) Begum, R.; Parida, M. R.; Abdelhady, A. L.; Murali, B.; Alyami, N. M.; Ahmed, G. H.; Hedhili, M. N.; Bakr, O. M.; Mohammed, O. F. Engineering Interfacial Charge Transfer in $CsPbBr_3$ Perovskite Nanocrystals by Heterovalent Doping. *J. Am. Chem. Soc.* **2017**, *139* (2), 731−737.

(19) Zhang, S.; Liu, H.; Li, X.; Wang, S. Enhancing quantum yield of $CsPb(Br_xCl_{1-x})_3$ nanocrystals through lanthanum doping for efficient blue light-emitting diodes. *Nano Energy* **2020**, *77*, 105302.

(20) Kim, Y. C.; An, H. J.; Kim, D. H.; Myoung, J. M.; Heo, Y. J.; Cho, J. H. High-Performance Perovskite-Based Blue Light-Emitting Diodes with Operational Stability by Using Organic Ammonium Cations as Passivating Agents. *Adv. Funct. Mater.* **2021**, *31* (5), 2005553.

(21) Chu, Z.; Zhao, Y.; Ma, F.; Zhang, C. X.; Deng, H.; Gao, F.; Ye, Q.; Meng, J.; Yin, Z.; Zhang, X.; You, J. Large cation ethylammonium incorporated perovskite for efficient and spectra stable blue light-emitting diodes. *Nat. Commun.* **2020**, *11* (1), 4165.

(22) Bi, C.; Wang, S.; Kershaw, S. V.; Zheng, K.; Pullerits, T.; Gaponenko, S.; Tian, J.; Rogach, A. L. Spontaneous Self-Assembly of Cesium Lead Halide Perovskite Nanoplatelets into Cuboid Crystals with High Intensity Blue Emission. *Advanced science* **2019**, *6* (13), 1900462.

(23) Wang, C.; Han, D.; Wang, J.; Yang, Y.; Liu, X.; Huang, S.; Zhang, X.; Chang, S.; Wu, K.; Zhong, H. Dimension control of in situ fabricated $CsPbClBr_2$ nanocrystal films toward efficient blue light-emitting diodes. *Nat. Commun.* **2020**, *11* (1), 6428.
(24) Cheng, L.; Yi, C.; Tong, Y.; Zhu, L.; Kusch, G.; Wang, X.; Wang, X.; Jiang, T.; Zhang, H.; Zhang, J.; Xue, C.; Chen, H.; Xu, W.; Liu, D.; Oliver, R. A.; Friend, R. H.; Zhang, L.; Wang, N.; Huang, W.; Wang, J. Halide Homogenization for High-Performance Blue Perovskite Electroluminescence. *Research* **2020**, *2020*, 9017871.
(25) Bi, C.; Yao, Z.; Sun, X.; Wei, X.; Wang, J.; Tian, J. Perovskite Quantum Dots with Ultralow Trap Density by Acid Etching-Driven Ligand Exchange for High Luminance and Stable Pure-Blue Light-Emitting Diodes. *Adv. Mater.* **2021**, *33* (15), 2006722.
(26) Yao, Z.; Bi, C.; Liu, A.; Zhang, M.; Tian, J. High brightness and stability pure-blue perovskite light-emitting diodes based on a novel structural quantum-dot film. *Nano Energy* **2022**, *95*, 106974.
(27) Liu, A.; Bi, C.; Tian, J. All Solution-Processed High Performance Pure-Blue Perovskite Quantum-Dot Light-Emitting Diodes. *Adv. Funct. Mater.* **2022**, *32* (44), 2207069.
(28) Luo, C.; Yan, C.; Li, W.; Chun, F.; Xie, M.; Zhu, Z.; Gao, Y.; Guo, B.; Yang, W. Ultrafast Thermodynamic Control for Stable and Efficient Mixed Halide Perovskite Nanocrystals. *Adv. Funct. Mater.* **2020**, *30* (19), 2000026.
(29) Cao, J.; Yan, C.; Luo, C.; Li, W.; Zeng, X.; Xu, Z.; Fu, X.; Wang, Q.; Chu, X.; Huang, H.; Zhao, X.; Lu, J.; Yang, W. Cryogenic-Temperature Thermodynamically Suppressed and Strongly Confined $CsPbBr_3$ Quantum Dots for Deeply Blue Light-Emitting Diodes. *Advanced Optical Materials* **2021**, *9* (17), 2100300.
(30) Hangleiter, A.; Hacker, R. Enhancement of band-to-band Auger recombination by electron-hole correlations. *Phys. Rev. Lett.* **1990**, *65* (2), 215−218.
(31) Klimov, V. V.; Mikhailovsky, A. A.; McBranch, D. W.; Leatherdale, C. A.; Bawendi, M. G. Quantization of multiparticle auger rates in semiconductor quantum dots. *Science* **2000**, *287* (5455), 1011−1013.
(32) Wang, Y.; Teng, Y.; Lu, P.; Shen, X.; Jia, P.; Lu, M.; Shi, Z.; Dong, B.; Yu, W. W.; Zhang, Y. Low Roll-Off Perovskite Quantum Dot Light-Emitting Diodes Achieved by Augmenting Hole Mobility. *Adv. Funct. Mater.* **2020**, *30* (19), 1910140.
(33) Zhang, J.; Jiang, L.; Huang, J.; Luo, X.; Luo, Z.; Zhou, D.; Kwok, H. S.; Xu, P.; Li, G. Unravelling the role of band-offset landscape on the recombination zone dynamics in perovskite light-emitting diodes. *Nano Select* **2021**, *2* (3), 624−631.
(34) Jiang, Y.; Cui, M.; Li, S.; Sun, C.; Huang, Y.; Wei, J.; Zhang, L.; Lv, M.; Qin, C.; Liu, Y.; Yuan, M. Reducing the impact of Auger recombination in quasi-2D perovskite light-emitting diodes. *Nat. Commun.* **2021**, *12* (1), 336.
(35) Yao, J. S.; Ge, J.; Wang, K. H.; Zhang, G.; Zhu, B. S.; Chen, C.; Zhang, Q.; Luo, Y.; Yu, S. H.; Yao, H. B. Few-Nanometer-Sized alpha-$CsPbI_3$ Quantum Dots Enabled by Strontium Substitution and Iodide Passivation for Efficient Red-Light Emitting Diodes. *J. Am. Chem. Soc.* **2019**, *141* (5), 2069−2079.
(36) Protesescu, L.; Yakunin, S.; Bodnarchuk, M. I.; Krieg, F.; Caputo, R.; Hendon, C. H.; Yang, R. X.; Walsh, A.; Kovalenko, M. V. Nanocrystals of Cesium Lead Halide Perovskites ($CsPbX_{(3)}$, X = Cl, Br, and I): Novel Optoelectronic Materials Showing Bright Emission with Wide Color Gamut. *Nano Lett.* **2015**, *15* (6), 3692−6.
(37) Dong, Y.; Qiao, T.; Kim, D.; Parobek, D.; Rossi, D.; Son, D. H. Precise Control of Quantum Confinement in Cesium Lead Halide Perovskite Quantum Dots via Thermodynamic Equilibrium. *Nano Lett.* **2018**, *18* (6), 3716−3722.
(38) Wei, K.; Zheng, X.; Cheng, X.; Shen, C.; Jiang, T. Observation of Ultrafast Exciton-Exciton Annihilation in CsPbBr3Quantum Dots. *Advanced Optical Materials* **2016**, *4* (12), 1993−1997.
(39) Quintero-Bermudez, R.; Sabatini, R. P.; Lejay, M.; Voznyy, O.; Sargent, E. H. Small-Band-Offset Perovskite Shells Increase Auger Lifetime in Quantum Dot Solids. *ACS Nano* **2017**, *11* (12), 12378−12384.
(40) Liu, F.; Ding, C.; Zhang, Y.; Kamisaka, T.; Zhao, Q.; Luther, J. M.; Toyoda, T.; Hayase, S.; Minemoto, T.; Yoshino, K.; Zhang, B.; Dai, S.; Jiang, J.; Tao, S.; Shen, Q. GeI_2 Additive for High Optoelectronic Quality $CsPbI_3$ Quantum Dots and Their Application in Photovoltaic Devices. *Chem. Mater.* **2019**, *31* (3), 798−807.
(41) Mondal, N.; Samanta, A. Complete ultrafast charge carrier dynamics in photo-excited all-inorganic perovskite nanocrystals ($CsPbX_3$). *Nanoscale* **2017**, *9* (5), 1878−1885.
(42) Luo, Y.; Tan, T.; Wang, S.; Pang, R.; Jiang, L.; Li, D.; Feng, J.; Zhang, H.; Zhang, S.; Li, C. Multivariant ligands stabilize anionic solvent-oriented alpha-$CsPbX_3$ nanocrystals at room temperature. *Nanoscale* **2021**, *13* (9), 4899−4910.
(43) Li, Y.; Lai, R.; Luo, X.; Liu, X.; Ding, T.; Lu, X.; Wu, K. On the absence of a phonon bottleneck in strongly confined $CsPbBr_3$ perovskite nanocrystals. *Chemical Science* **2019**, *10* (23), 5983−5989.
(44) Wu, K.; Liang, G.; Shang, Q.; Ren, Y.; Kong, D.; Lian, T. Ultrafast Interfacial Electron and Hole Transfer from $CsPbBr_3$ Perovskite Quantum Dots. *J. Am. Chem. Soc.* **2015**, *137* (40), 12792−5.
(45) Zhu, Y.; Zhao, J.; Yang, G.; Xu, X.; Pan, G. Ammonium acetate passivated $CsPbI_3$ perovskite nanocrystals for efficient red light-emitting diodes. *Nanoscale* **2020**, *12* (14), 7712−7719.
(46) Zhou, L.; Liao, J. F.; Qin, Y.; Wang, X. D.; Wei, J. H.; Li, M.; Kuang, D. B.; He, R. Activation of Self-Trapped Emission in Stable Bismuth-Halide Perovskite by Suppressing Strong Exciton−Phonon Coupling. *Adv. Funct. Mater.* **2021**, *31* (31), 2102654.
(47) Yang, S.; Bi, C.; Dong, W.; Zhang, X.; Zheng, W.; Choy, W. C. H.; Tian, J. Electron Delocalization in $CsPbI_3$ Quantum Dots Enables Efficient Light-Emitting Diodes with Improved Efficiency Roll-Off. *Advanced Optical Materials* **2022**, *10* (11), 2200189.
(48) Song, J.; Fang, T.; Li, J.; Xu, L.; Zhang, F.; Han, B.; Shan, Q.; Zeng, H. Organic-Inorganic Hybrid Passivation Enables Perovskite QLEDs with an EQE of 16.48. *Adv. Mater.* **2018**, *30* (50), 1805409.
(49) Bae, W. K.; Park, Y. S.; Lim, J.; Lee, D.; Padilha, L. A.; McDaniel, H.; Robel, I.; Lee, C.; Pietryga, J. M.; Klimov, V. I. Controlling the influence of Auger recombination on the performance of quantum-dot light-emitting diodes. *Nat. Commun.* **2013**, *4*, 2661.

https://doi.org/10.1021/acsenergylett.2c02613
ACS Energy Lett. 2023, 8, 731−739